Nano Research
2023, 16(8): 11473–11485

ISSN 1998-0124 CN 11-5974/O4
https://doi.org/10.1007/s12274-023-5795-7

Research Article

Single-atomic Zn-(C/N/O) lithiophilic sites induced stable lithium plating/stripping in anode-free lithium metal battery

Shifei Huang[1,2], Sirong Lu[3], Yao Lv[1,4], Nanrui Li[1,2], Zhenwei Wu[5], Geng Zhong[1,2], Xiaolong Ren[1,2], Yufeng Wang[1,2], Bo Sun[1,2], Yuxiong Huang[2,6], Feiyu Kang[1,2] (✉), and Yidan Cao[1,2] (✉)

[1] *Institute of Materials Research, Tsinghua Shenzhen International Graduate School, Tsinghua University, Shenzhen 518055, China*
[2] *Tsinghua-Berkeley Shenzhen Institute, Tsinghua Shenzhen International Graduate School, Tsinghua University, Shenzhen 518055, China*
[3] *Shenzhen Institute for Quantum Science and Engineering, Southern University of Science and Technology, Shenzhen 518055, China*
[4] *College of Sciences and Institute for Sustainable Energy, Shanghai University, Shanghai 200444, China*
[5] *Shell Catalysts & Technologies, Shell Technology Center Houston, Houston TX 77082-3101, USA*
[6] *Institute of Environment and Ecology, Tsinghua Shenzhen International Graduate School, Tsinghua University, Shenzhen 518055, China*

Received: 23 March 2023 / **Revised:** 29 April 2023 / **Accepted:** 1 May 2023

ABSTRACT

For anode-free lithium metal battery, lithiophilic surface modification on the current collector can effectively reduce the lithium nucleation barrier, so as to regulate the electrodeposition of lithium. Here, atomically dispersed Zn-(C/N/O) lithiophilic sites in the amorphous carbon medium were introduced onto Cu by an *in-situ* induced ion coordination chemistry strategy to get the modified Zn@NC@RGO@Cu current collector. X-ray absorption spectroscopy (XAS) combined with scanning transmission electron microscopy in high angle annular dark field (STEM-HAADF) analysis proved the single atomic state of the zinc sites surrounded by C, N, and O with a coordination number of ~ 3. According to the electrochemical tests and first principle calculations, the ultra-uniformly dispersed Zn-(C/N/O) sites at the atomic level can effectively improve the lithium affinity, reduce the energy barrier for lithium nucleation, homogenize the lithium nucleation, and enhance an inorganic lithium compounds rich solid electrolyte interphase layer. As a result, the nucleation overpotential of lithium on the modified current collector was reduced to 7.7 mV, which was 5.4 times lower than that on bare Cu. Uniform lithium nucleation and deposition enabled stable Li plating/stripping and elevated Coulombic efficiency of 98.95% in Li||Cu cell after > 850 cycles. Capacity retention of 89.7% was successfully achieved in the anode-free lithium metal battery after 100 cycles.

KEYWORDS

single atomic zinc, carbon, lithiophilic sites, lithium dendrite, anode-free

1 Introduction

With the wide application and rapid development of lithium-ion batteries in electric vehicles and portable devices, it is highly demanded to develop batteries with higher energy density, improved safety performance, longer lifetime, and lower cost [1, 2]. At present, the energy density of commercial lithium-ion battery is approaching its theoretical limit (350 Wh·kg^{-1}) and it is more and more challenging to further improve the energy density, which has become a key factor restricting the development of energy storage devices [3–5]. Lithium metal possesses extremely high theoretical capacity of 3860 mAh·g^{-1}, ten times that of graphite (372 mAh·g^{-1}) [6], and low redox potential (−3.04 V vs. standard hydrogen electrode) [7]. Replacing graphite-based anode with metallic lithium is one of the most promising strategies to improve the energy density of rechargeable lithium-ion battery to achieve the goal of 400 Wh·kg^{-1} or even higher energy densities [8–10]. However, the excessive usage of lithium (N/P > 10) in lithium metal battery greatly reduces the real energy density. And many problems, including uncontrollable lithium deposition, dendrite growth, electrode volume change, severe interfacial reaction with electrolyte, and "dead lithium" formation, also severely diminish the lifetime of the battery and may lead to thermal runaway and other safety problems [11, 12].

Numerous strategies have been studied to mitigate the above mentioned problems associated with lithium metal anode, including current collector engineering [13], separator modification [14, 15], artificial solid electrolyte interface (SEI) [16], electrolyte modification [17–19], etc. The strategy around current collector is also powerful for developing zero excess lithium or lithium-free rechargeable batteries, which is called anode-free lithium metal batteries (AFLMBs) [20]. This new battery system is expected to greatly increase the energy density by more than 40% compared with the existing lithium-ion battery. At the same time, the usage of lithium metal foil can be avoided in the fabrication process, which provides great convenience, reduces the cost, and improves the safety. In the AFLMB configuration, the anode begins as a bare current collector and lithium metal is *in-situ* plated from the cathode on the initial plating step. Therefore, the lithium affinity and uniformity of nucleation sites are important factors affecting the electrochemical deposition of lithium on the current collector [12]. The Cu current collector with face-centered

Address correspondence to Yidan Cao, yidancao@sz.tsinghua.edu.cn; Feiyu Kang, fykang@sz.tsinghua.edu.cn

cubic (FCC) crystal structure, is one of the most unfavorable deposition substrates for lithium metal with body-centered cubic (BCC) crystal structure due to the largest crystal mismatch, which leads to high nucleation overpotential and uneven deposition [11, 21, 22]. Lithiophilic materials like liquid metal [23], silicon oxide [24], transition metal compound [25], polymer [26], carbon [27], and alloy [28], which promote uniform and compact Li nucleation/growth, have been used for surface modification on Cu current collector.

Carbon-based material with high electrochemical stability is an ideal candidate for current collector modification to induce uniform lithium deposition [29, 30]. The microstructure of carbon is quite controllable and can be lithium affinitive with proper modification [31]. A variety of carbon-based materials, including carbon nanotubes [32], graphite/graphited carbon [33], graphene [34], and graphene oxides (GOs) and reduced GOs (RGOs) [35], have been applied to regulate the deposition behavior of Li metal. Chen et al. [31] reported that carbon with precise O, N, and B functional doping could significantly reduce the Li nucleation overpotential. O doping results in the most improved lithiophilicity among single-doped carbons, but excessive introduction of oxygen in carbon materials will impair the conductivity. There are three forms of N doping, among which pyridine N dominates in improving lithium affinity and inducing uniform lithium nucleation/growth [36, 37]. Besides, transition metals, like Zn [38] and Ag [39], have been investigated as nucleation sites for lithium and combined with carbon-based materials to regulate lithium plating/stripping behavior [40, 41]. Wang et al. [42] used nitrogen doped carbon spheres loaded with silver nanoparticles to regulate lithium deposition, however, silver nanoparticles would aggregate seriously after long-term cycling and exhibit poor stability. Although some methods have been proposed to synthesize lithiophilic carbon host, the precise control of doping in carbon host is still challenging.

Here in this work, atomically dispersed lithiophilic zinc sites are introduced into O/N co-doped carbon nanolayer on Cu current collector (Zn@NC@RGO@Cu) through the metal ion-dopamine (DA) coordination strategy. The ultra-uniformly dispersed single atomic lithiophilic Zn-(C/N/O) sites work synergistically with the carbon nanolayer and effectively reduce the overpotential of lithium nucleation, resulting in homogeneous lithium nucleation and compact dendrite-free lithium deposition. As a result, stable dendrite-free cycling for more than 200 cycles is achieved with elevated Coulombic efficiency (CE) and capacity retention in anode-free lithium metal battery.

2 Results and discussion

2.1 Characterization of modified current collector

The modified Cu current collector was fabricated through GO induced crosslinking of DA together with *in-situ* coordination between dopamine and Zn^{2+}. Typically, GO coated Cu foil, which consists of oxygen-containing functional groups like carboxyl (–COOH) and epoxy (C–O–C) groups (box ① in Fig. 1(a)), was immersed in DA tris-HCl buffer solution, to induce the uniform crosslinking of DA by imino groups (–NH–) and peptide bonds (–CONH–) (box ② in Fig. 1(a)), getting PDA layer coated GO@Cu precursor (PDA@GO@Cu). Zn^{2+} containing DA tris-HCl buffer solution was used to prepare Zn^{2+}-PDA coated Zn@PDA@GO@Cu. The catechol group in dopamine is a strong ligand for many multivalent metal cations, Zn^{2+} in its matrix (box ③ in Fig. 1(a)). The –NH– stretching vibration (3406 cm^{-1}) and –CONH– groups (1537 cm^{-1}) due to crosslinking as well as some other oxygen-containing and nitrogen containing functional groups from dopamine were detected in the synthesized PDA@GO@Cu and Zn@PDA@GO@Cu by Fourier transform infrared (FTIR) spectroscopy (Fig. 1(b)), confirming the occurrence of the crosslinking. Additionally, the bands around 1510 and 1604 cm^{-1} in Fig. 1(c) are attributed to the stretching vibration of the indole and indoline groups in the PDA layer. For the Zn@PDA@GO@Cu, the band around 1510 cm^{-1} is split into two bands at 1497 and 1541 cm^{-1}, and the band around 1604 cm^{-1} shifts to 1617 cm^{-1} due to the interaction between zinc ion and PDA, indicating the formation of Zn^{2+}-PDA complex [43–46]. The prepared samples were pyrolyzed in argon to carbonize PDA and reduce GO, and modification layers with N-doped carbon medium (NC) on RGO (NC@RGO and Zn@NC@RGO) could be obtained. The carbon medium modified layer is rich in oxygen and nitrogen, which can greatly improve the lithiophilicity of the carbon substrate [31]. Moreover, the introduction of lithiophilic Zn [47], the amount of which was determined to be 0.94 wt.% by ICP test, in the carbon medium is expected to reduce the nucleation barrier of lithium and facilitate uniform lithium plating.

The microstructures of the samples were characterized by X-ray diffraction (XRD), Raman spectroscopy, and electron microscopy. As shown in Fig. S1(a) in the Electronic Supplementary Material (ESM), a broad peak at ~ 22°, which is the (002) diffraction pattern of disordered carbon, demonstrates the amorphous feature of the carbon medium. There is an overlap of diffraction peaks from carbon medium and Cu substrate at high angles, as indicated in Fig. S1(a) in the ESM. Peaks corresponding to D-band (defect) and G-band (E_{2g} lattice vibration) show up at 1347.5 and 1597.4 cm^{-1}, respectively, in the Raman spectra (Fig. S1(b) in the ESM). The I_D/I_G values are 0.84 and 0.85 in NC@RGO@Cu and Zn@NC@RGO@Cu, respectively, indicating that there are abundant defects in the carbon medium layer due to the low degree of crystallization and the introduction of heterogeneous elements.

Scanning electron microscopy (SEM) and high-resolution transmission electron microscopy (HRTEM) images were collected to observe the morphology and microstructure of the surface layer on Cu foil. The rough surface of bare Cu foil (Fig. 2(a)) is covered by a smooth and compact layer with 80–350 and 70–120 nm nanoparticles after the introduction of carbon medium in NC@RGO@Cu and Zn@NC@RGO@Cu, respectively (Figs. 2(b) and 2(c)). The evenly distributed nanoparticles are aggregated carbon formed by the *in-situ* growth of amine during pyrolysis, and the composition of the nanoparticles is consistent with the rest of the modification layer (Fig. S2 in the ESM). By contrast, there are a lot of cracks in the modification layer on NC@Cu and Zn@NC@Cu, which were prepared by a similar method on the substrates without GO (Fig. S3 in the ESM). It demonstrates that the introduction of GO can enhance the toughness of the crosslinked PDA layer to avoid formation of cracks and peel-off of the carbon medium layers. The thickness of the modification layer in NC@RGO@Cu and Zn@NC@RGO@Cu is 650 and 600 nm, respectively (Figs. 2(e) and 2(f)), which is only about one fifteenth of the thickness of Cu foil (Fig. 2(d)). The nano thin layer provides a uniform substrate for lithium deposition and does not substantially increase the weight and volume of the current collector, which may be beneficial to the application in lithium metal batteries, especially in anode-free lithium metal batteries. The HRTEM images show that the modification layer consists of nanopores surrounded by disordered carbon in NC@RGO@Cu (Fig. 2(g)) and Zn@NC@RGO@Cu (Fig. 2(i)). No long-range ordered crystalline structures are found in the samples from the selected area electron diffraction (SAED) patterns and the carbon media in the sample

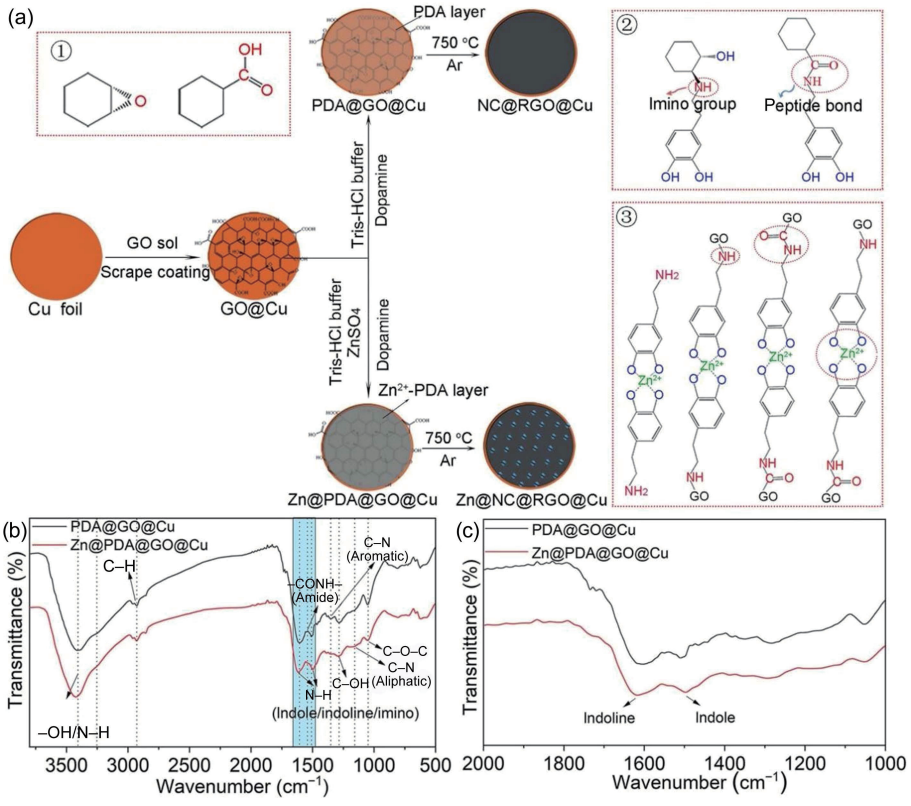

Figure 1 (a) Schematic diagram of the synthesis process of NC@RGO@Cu and Zn@NC@RGO@Cu current collector. (b) and (c) FTIR spectroscopy curves of PDA@GO@Cu and Zn@PDA@GO@Cu.

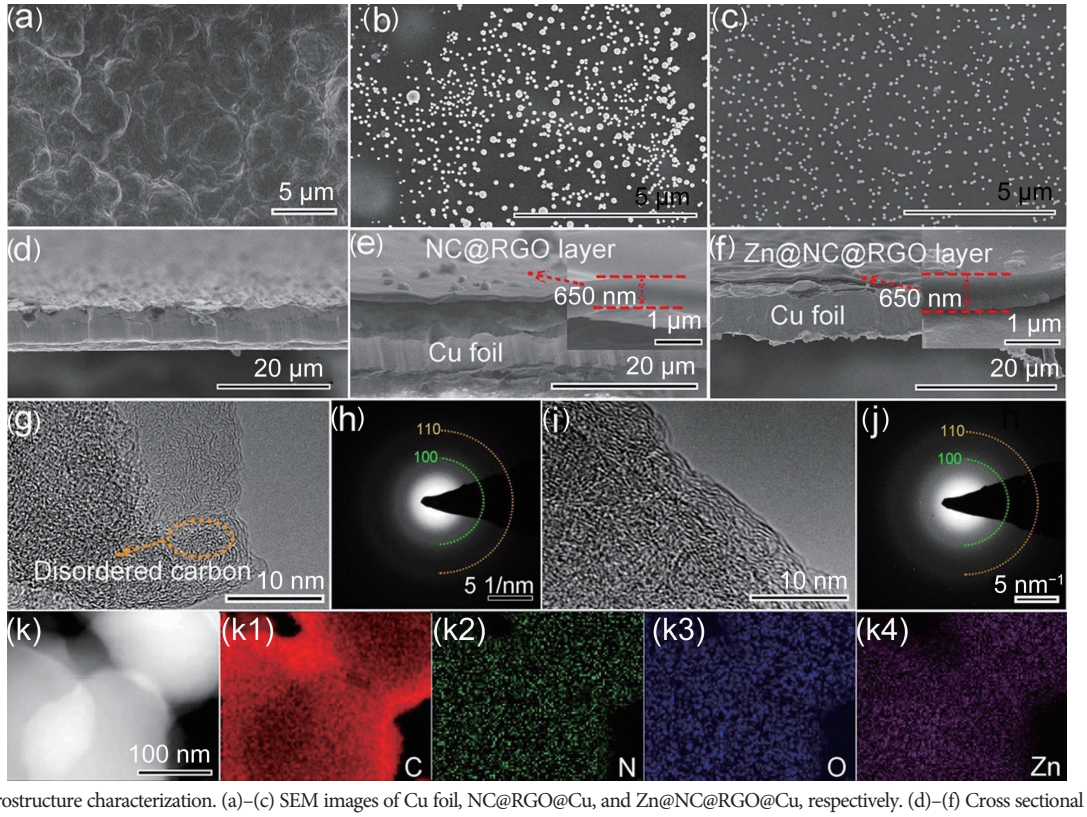

Figure 2 Microstructure characterization. (a)–(c) SEM images of Cu foil, NC@RGO@Cu, and Zn@NC@RGO@Cu, respectively. (d)–(f) Cross sectional images of Cu foil, NC@RGO@Cu, and Zn@NC@RGO@Cu, respectively. (g) and (h) HRTEM and corresponding SAED images of NC@RGO@Cu. (i) and (j) HRTEM and corresponding SAED images of Zn@NC@RGO@Cu. (k) The STEM-HAADF image of the modified layer on Zn@NC@RGO@Cu, and (k1)–(k4) the corresponding element mapping images of C, N, O, and Zn.

are fully amorphous in the HRTEM images. Weak diffraction rings with ring sizes of 0.21 and 0.12 nm coincide with reported amorphous carbon and CN_x films [48, 49]. And (002) diffraction ring cannot be distinguished, indicating the low degree of crystallization. It confirms the amorphous nature of carbon medium in the modification layer, which agrees well with the XRD and Raman analysis. The scanning transmission electron microscopy in high angle annular dark field (STEM-HAADF) images of the modification layer in Zn@NC@RGO@Cu show that the C, N, O, and Zn elements are homogeneously distributed over

the entire layer (Fig. 2(k)), and isolated Zn atoms are well-dispersed over the sample. The local coordination structure and chemical states of the heteroatoms in the modification layer of Zn@NC@RGO@Cu were characterized by X-ray photoelectron spectroscopy (XPS) and X-ray absorption spectroscopy (XAS). XPS analyses show that the contents of C, O, N, and Zn in the modification layer of Zn@NC@RGO@Cu are 85.88 at.%, 8.65 at.%, 5.23 at.%, and 0.24 at.%, respectively, and those are 83.96 at.% (C), 10.69 at.% (O), and 5.35 at.% (N) in the NC@RGO@Cu (Fig. S4(a) in the ESM). The peaks at 284.7, 285.7, 286.2, and 288.9 eV in the C 1s spectra (Figs. S4(b) and S4(c) in the ESM) correspond to C–C, C–N, C–O, and O–C=O, respectively [50]. Among them, C–C is the skeleton of the modification layer that originates from the amorphous carbon. C–N, C–O, and O–C=O sites can effectively enhance the lithium affinity of carbon matrix [31]. The amount of C–N in Zn@NC@RGO@Cu (Fig. S4(b) in the ESM) is similar to that in NC@RGO@Cu (Fig. S4(c) in the ESM), suggesting that the introduction of a small amount of Zn in the carbon layer does not significantly affect the chemical states of C and N. For the N 1s spectra in NC@RGO@Cu (Fig. S4(d) in the ESM), there are four peaks attributed to pyridine N (398.4 eV), pyrrolidine N (400.8 eV), graphite N (402 eV), and N–O (403.2 eV), respectively [51]. By contrast, besides the peaks of pyridine N (398.4 eV), pyrrolidine N (400.8 eV), graphite N (402 eV), and N–O (403.4 eV), an additional peak shows up at 399.8 eV in Zn@NC@RGO@Cu (Fig. 3(a)), which is related to the Zn-N(O)$_x$ coordination [51]. The contents of nitrogen-containing functional groups pyridinic N and N–O, which possess good lithium affinity [31], in Zn@NC@RGO@Cu (1.92% and 0.69%) are higher than those in NC@RGO@Cu (1.73% and 0.23%) (Figs. S4(f) and S4(g) in the ESM). The pyrrolic N and graphitic N in carbon materials are also lithiophilic only when accompanied with rich defect sites [31, 52]. The introduction of Zn leads to the formation of Zn-N(O)$_x$ coordination, a new lithiophilic site in the carbon media, which will be further verified in the subsequent analysis. The peaks corresponding to C=O, C–OH, C–O–C, and COOH are found at 531.3, 532.3, 533.3, and 535 eV in the O 1s spectra (Fig. 3(b) and Fig. S4(e) in the ESM). The percentage of the oxygen related peaks in Figs. S4(h) and S4(i) in the ESM show that the content of

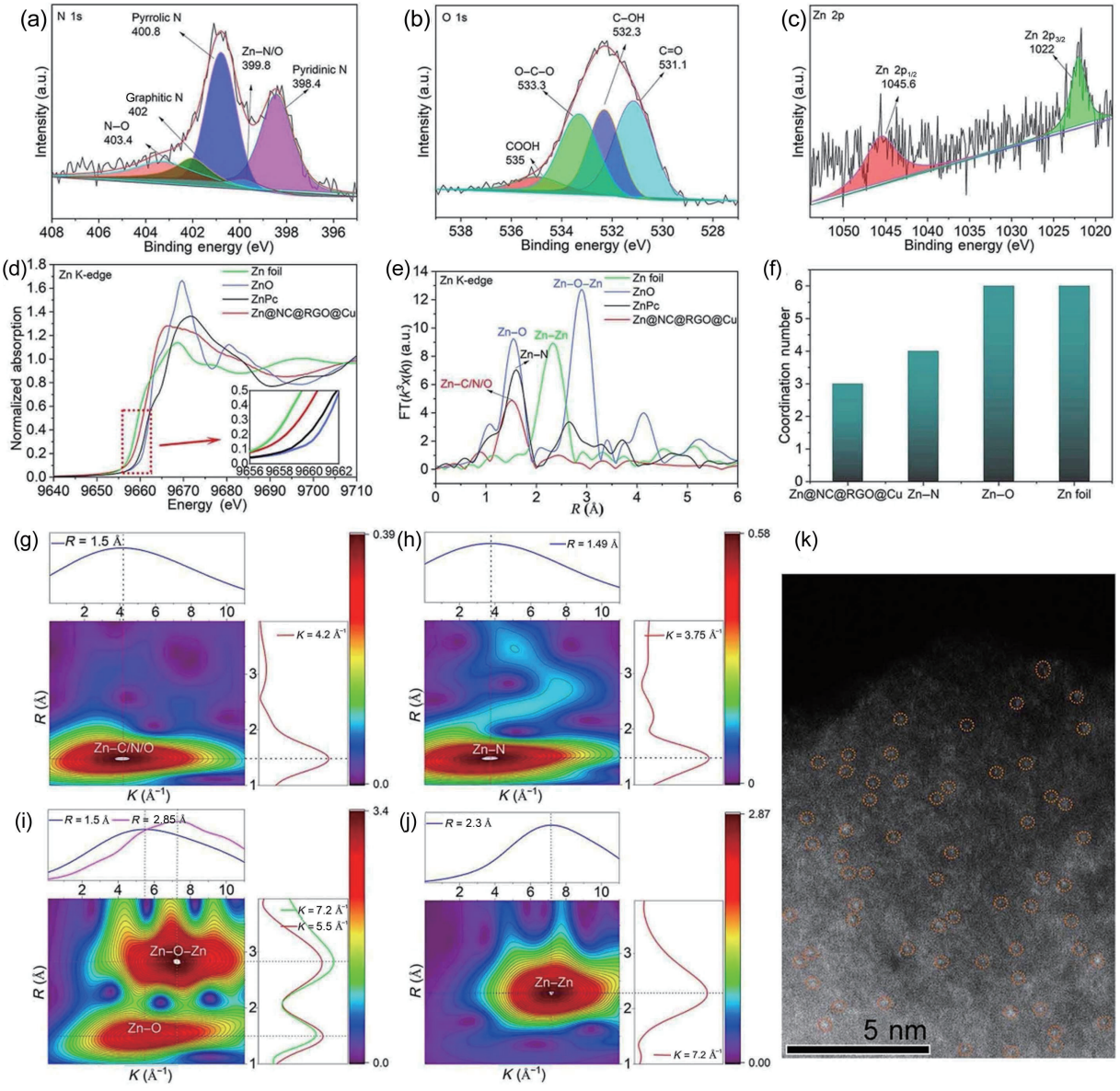

Figure 3 Deconvoluted XPS spectra of (a) N 1s, (b) O 1s, and (c) Zn 2p in Zn@NC@RGO@Cu. (d) The normalized XANES curves (inset: enlarged view), (e) Fourier transform k^3-weighted extended (R space) EXAFS curves at the Zn K-edge, and (f) the coordination number of zinc in the modification layer of Zn@NC@RGO@Cu, ZnPc, ZnO, and Zn foil, respectively. (g)–(j) The wavelet transform spectra of Zn@NC@RGO@Cu, ZnPc, ZnO, and Zn foil, respectively. (k) Spherical aberration corrected atomic-resolution HAADF-STEM image, in which the bright dots are Zn single atoms, some of which are highlighted by yellow circles.

lithiophobic C–OH in Zn@NC@RGO@Cu is significantly less than that in NC@RGO@Cu, while the contents of C=O, C–O–C, and COOH with good lithium affinity are significantly increased [5, 40, 52].

There is only one existing chemical state of zinc according to the Zn 2p spectra in Zn@NC@RGO@Cu (Fig. 3(c)). Zn K-edge X-ray absorption near-edge structure (XANES) spectra (Fig. 3(d)) show that the Zn@NC@RGO@Cu sample has a leading edge that rises at an energy value higher than Zn foil but lower than ZnO or ZnPc. When determining its edge energy from the maximum of the first derivative of the XANES (Fig. S5(a) in the ESM), multiple maxima could be seen including one at 9660.5 eV, one at 9662.6 eV, and likely another feature around 9661.7 eV. While typically the first maximum in the XANES first derivative is taken as the edge energy of the sample, the Zn@NC@RGO@Cu sample shows a very wide peak in the XANES first derivative that is a result of the overlap of multiple features likely originated from the different components of the sample. The first maximum at 9660.5 eV is 1.5 eV higher than the Zn foil edge energy, consistent with the value reported for diethylzinc grafted on silica [53], which also has a XANES leading edge that rises at energy lower than ZnO and ZnPc due to Zn–C bonding with the ethyl group that is much less electro-negative than O and N containing ligands. The last maximum at 9552.6 eV is 3.6 eV higher than the Zn foil, the same as the literature report for Zn(II) on silica, containing Zn with tetrahedral Zn–O bonds [53]. The other feature in the XANES first derivative at around 9661.7 eV has a similar edge energy compared to ZnO and ZnPc. Overall, the XANES indicates that the zinc component in Zn@NC@RGO@Cu has an oxidation state of +2, and exists in Zn-C/N/O coordinations. The FT spectra of the Zn K-edge k^3-weighted extended X-ray absorption fine structure (EXAFS) spectra (Fig. 3(e)) in Zn@NC@RGO@Cu exhibit only one shell scattering peak at 1.50 Å (phase-uncorrected distance), which is similar to that of Zn–C (~ 1.5 Å) in diethylzinc [53], Zn–N (1.58 Å) in ZnPc, and Zn–O (1.53 Å) in ZnO. These suggest that the shell scattering is attributed to the Zn–C/N/O bond rather than the Zn–Zn bond at higher distance regions (> 2 Å) [54]. The coordination parameters in Fig. 3(f) and Table S1 in the ESM were derived from the quantitative analysis of the Zn K-edge EXAFS fitting (Figs. S5(b)–S5(d) in the ESM). The coordination number of the Zn in Zn@NC@RGO@Cu is around 3.2 ± 0.2 Å and the bond length of Zn–C/N/O is 1.97 ± 0.1 Å. Therefore, the configuration of Zn atom in carbon matrix should be Zn-(C/N/O). The respective coordination numbers of Zn–C, Zn–N, or Zn–O cannot be accurately determined since the bond lengths of Zn–C, Zn–N, and Zn–O as well as the atomic number of carbon, nitrogen, and oxygen are similar.

The EXAFS spectra were further subjected to wavelet transform (WT) to distinguish the contributions of different scattering in *K* space (Figs. 3(g)–3(j)). In *R* space, we can only see which positions have peaks and the height of the peaks, but we cannot judge which coordination elements the peaks correspond to. Different coordination elements have different *K* space oscillation modes. For lighter elements, the strongest oscillation in *K* space occurs at a lower wave number; for the heavier elements, the strongest oscillation in *K* space occurs at the higher wavenumber position. Different from the two-dimensional information in *R* space obtained by Fourier transform, wavelet analysis can combine *R* space and *K* space to obtain three-dimensional information, which can effectively analyze data and obtain more reliable results. As shown in Fig. 3(g), only one lobe is visible with the maximum intensity at 4.2 $Å^{-1}$ in *K* space and at 1.5 $Å^{-1}$ in *R* space in the Zn@NC@RGO@Cu, which is an overlap of the Zn–C, Zn–N (3.75 $Å^{-1}$ in *K* space and 1.49 $Å^{-1}$ in *R* space, Fig. 3(h)) and Zn–O (5.5 $Å^{-1}$ in *K* space and 1.5 $Å^{-1}$ in *R* space, Fig. 3(i)). Compared with ZnO (Fig. 3(i)) and Zn foil (Fig. 3(j)), the feature of Zn–Zn lobe does not show up in the Zn@NC@RGO@Cu, suggesting the single atomic state of the zinc atoms [54, 55]. The spherical aberration corrected atomic-resolution HAADF-STEM image of Zn@NC@RGO@Cu (Fig. 3(k)) shows bright dots identified as the atomically dispersed Zn in the carbon matrix, which is consistent with the above XAS analysis and the HAADF-STEM elemental mapping results in Fig. 2(k).

2.2 Electrochemical evaluation of Li||Cu half-cells

The lithium plating/stripping behavior on different current collectors was investigated to probe the superiority of the Zn@NC@RGO@Cu. As shown in the initial lithium plating voltage profiles recorded at 0.1 $mA·cm^{-2}$ in Fig. 4(a), the nucleation overpotentials (η_n) in the nucleation regime of lithium on NC@RGO@Cu and Zn@NC@RGO@Cu are 10.5 and 7.7 mV, respectively, which are much lower than that on Cu foil (41.7 mV). Nucleation overpotential is related to the energy barrier of Li deposition on heterogeneous substrates, which can reveal the lithiophilic property of the substrates [56–58]. The reduced overpotential on NC@RGO@Cu indicates that the doped carbon nanolayers on Cu foil effectively reduce the lithium deposition energy barrier. Moreover, the uniform introduction of single atomic lithiophilic zinc-coordination sites further improves the lithiophilicity of the substrate. It is worth noting that the overpotential of NC@RGO@Cu and Zn@NC@RGO@Cu appears later than that of Cu. This delay can be attributed to the amorphous carbon in the modified layer, which allows for lithium storage through adsorption and intercalation before lithium plating, and the lithiated carbon media can contribute as lithiophilic sites during cycling [59, 60]. After the initial Li nucleation, the overpotential slowly increases to η_p (plating overpotential) and enters the lithium growth regime with the progress of lithium plating, since the energy barrier of lithium deposition on the nucleated sites is lower than that of new nuclei formation. The absolute value of η_p on Zn@NC@RGO@Cu (6 mV) is less than those on NC@RGO@Cu (6.9 mV) and Cu foil (7.5 mV), which suggests a lower charge transfer resistance in Zn@NC@RGO@Cu. The significantly increased lithium nucleophilic sites due to the introduction of single atomic lithiophilic zinc-coordination sites result in the reduced energy barrier for lithium nucleation and growth on Zn@NC@RGO@Cu, which plays a vital role in promoting stable lithium plating/stripping in the subsequent cycling.

As shown in the voltage profiles of Li||Cu half cells in Fig. S6(a) in the ESM, the Zn@NC@RGO@Cu current collector stably cycles for > 4720 h, which is way longer than that of NC@RGO@Cu (3250 h) and bare Cu (~ 1500 h) current collectors. Meanwhile, the voltage hysteresis (Fig. 4(b)) on bare Cu fluctuates severely and quickly exhibits cycling fade. By contrast, the modified current collectors, especially Zn@NC@RGO@Cu, show more stable voltage hysteresis and cycling stability. Hysteresis voltage is an important index to reflect the voltage polarization and internal resistance in the process of lithium deposition and stripping. The hysteresis voltages of all the electrodes decrease after several cycles in Fig. 4(b), which is related to the facilitated charge transfer due to the formation of SEI layer. As revealed in Figs. 4(c)–4(f), the hysteresis voltage on bare Cu (Fig. 4(c)) is 45.9 mV after the two formation cycles, and it remains around 22.4 to 23.2 mV during the subsequent cycles before it suddenly rises to 38.8 mV at the 400th cycle. The huge increase of hysteresis on bare Cu implies the formation of a highly resistive interfacial layer consisting of dead Li and decomposed electrolyte. The initial hysteresis voltages on NC@RGO@Cu (Fig. 4(d)) and Zn@NC@RGO@Cu (Fig. 4(e)) are reduced to 29.6 and 27.4 mV, indicating that the modification

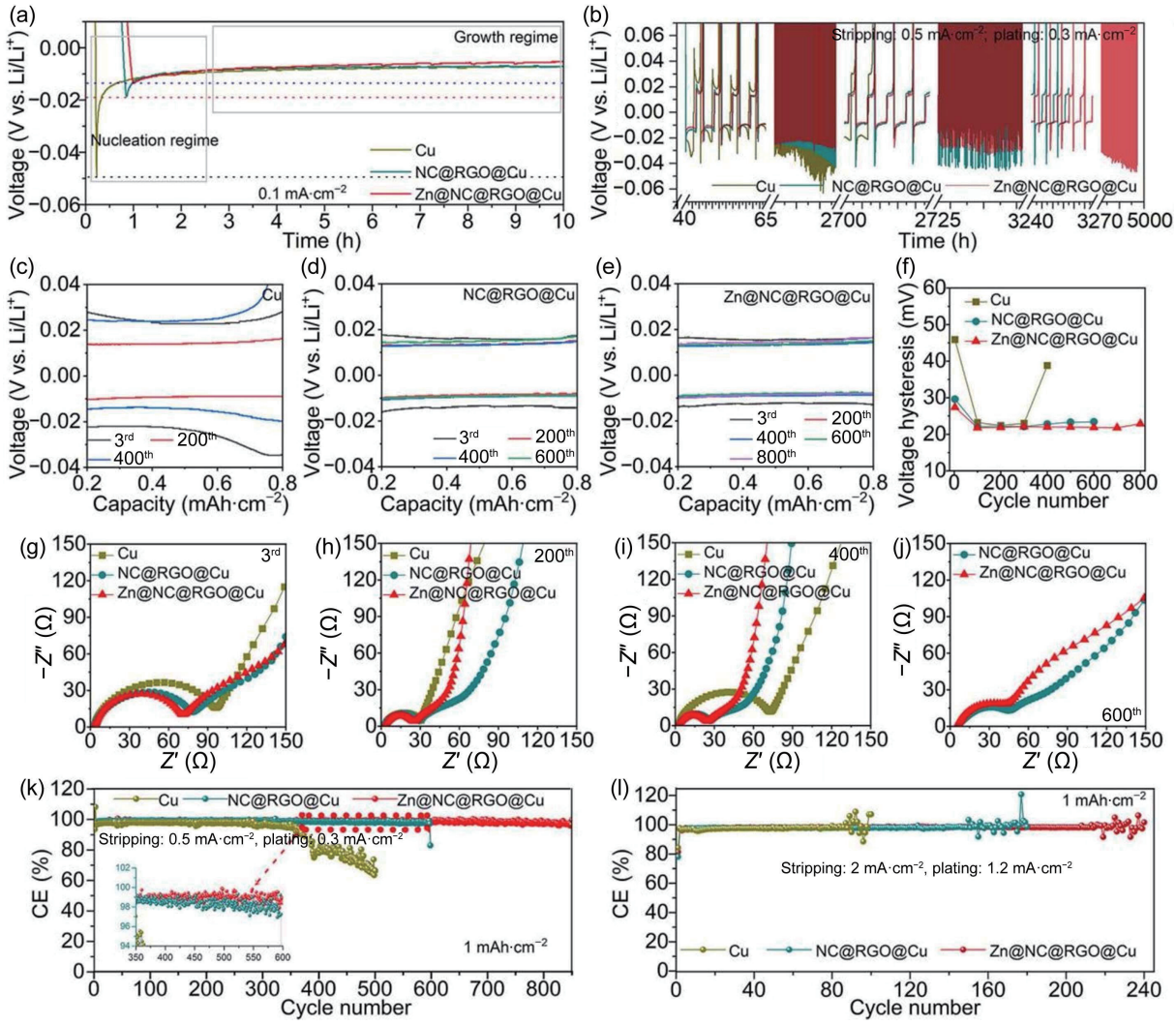

Figure 4 Electrochemical evaluation of Cu foil, NC@RGO@Cu, and Zn@NC@RGO@Cu electrode in anode half-cells. (a) Voltage–time profiles recorded during lithium plating at 0.1 mA·cm^{-2} at the first cycle. (b) Magnified voltage–time profiles of the Li plating at 0.3 mA·cm^{-2}/stripping at 0.5 mA·cm^{-2} with a cycling capacity of 1 mAh·cm^{-2} (after two cycles activation at 0.1 mA·cm^{-2}), and (c)–(e) corresponding voltage hysteresis curves during the 3rd, 200th, 400th, 600th, and 800th cycle, (f) variation trend of hysteresis voltage with the number of cycles, (g)–(j) EIS curves during the 3rd, 200th, 400th, and 600th cycle, respectively, and (k) variation trend of CEs and charge–discharge specific capacity with the number of cycles. (i) CEs and charge–discharge specific capacity curves at the current densities of the Li plating at 1.2 mA·cm^{-2}/stripping at 2 mA·cm^{-2} for a total capacity of 1 mAh·cm^{-2}.

layer can effectively reduce the interfacial resistance. The hysteresis voltage on NC@RGO@Cu gradually increases after 400 cycles, while the hysteresis voltage on Zn@NC@RGO@Cu remains unchanged until the 800th cycle, indicating much lower internal resistance in the cell with Zn@NC@RGO@Cu current collector.

Electrochemical impedance spectroscopy (EIS) was employed to understand the interfacial charge transfer behavior and the evolution of hysteresis voltage. The SEI film formed on the electrode surface is the main factor affecting the transmission dynamics of lithium ion at the interface. The interfacial resistance is 92.5, 72.6, and 66.8 Ω in Cu foil, NC@RGO@Cu, and Zn@NC@RGO@Cu, respectively, after the initial formation cycles (Fig. 4(g)). The interfacial impedance gradually decreases and charge transfer is facilitated in the subsequent cycles as stable SEI is formed (Fig. 4(h)). It is worth noting that the interfacial impedance increases greatly before the short circuit of Li||Cu cell (Fig. 4(i)), which is due to the accumulation of resistive SEI and dead lithium caused by continuous side reactions between lithium and electrolyte [58]. By contrast, the modification layer on Cu effectively reduces the interfacial resistance during cycling, improves the kinetics of Li deposition and stripping, and prolongs the cycle stability, especially for the Zn modified layer (Fig. 4(j)). As a result, the Li||Zn@NC@RGO@Cu cell exhibits an average CE (ACE) of 98.95%, with stable cycling for > 850 cycles (Fig. 4(k)). In contrast, the ACE of Li||bare Cu is 97.74% with fluctuating cycling for 280 cycles and obvious attenuation appears after ~ 350 cycles. It is related to the generation of massive lithium dendrites and continuous consumption of active lithium and electrolyte due to side reactions on the surface of the electrode [57]. Compared with Cu foil, Li||NC@RGO@Cu achieves a higher ACE of 98.31% for 600 cycles, and a gradual decline of CE shows up after 350 cycles (inset in Fig. 4(k)). The rapid decrease of CE after 350 cycles is mainly attributed to the significant accumulation of dead lithium or local micro short circuits caused by lithium branches during the cycling process [61]. The Zn@NC@RGO@Cu also exhibits excellent electrochemical performance at higher currents and capacities. With the increase of the Li plating/stripping current density to 1.2 mA·cm^{-2}/2 mA·cm^{-2}, the Li||Zn@NC@RGO@Cu cell still stably cycles for ~ 215 cycles with an ACE of 98.3%, which is much higher than Li||NC@RGO@Cu cell for 150 cycles with an ACE of 98.06% and Li||Cu cell for 86 cycles with an ACE of 97.44% (Fig. 4(l) and Fig. S6(b) in the ESM). It is worth noting that before the battery completely fails, high stripping current increases the recovery rate of dead lithium, and the formation and revival of dead lithium lead to fluctuations of CE [62]. The Li deposition amount is further increased to 2 and 4 mAh·cm^{-2}, and

the prepared Zn@NC@RGO@Cu current collector can still maintain the cycle stability of > 450 cycles and > 150 cycles, respectively (Figs. S6(c) and S6(d) in the ESM). The growth of Li dendrite is directly related to the current density. High current density will accelerate the growth of lithium dendrites and the cell failure [63]. The excellent electrochemical performance of the Li||Zn@NC@RGO@Cu cell at various current densities suggests that the single atomic zinc-coordination rich lithiophilic modification layer effectively improves the Li plating/stripping stability as well as lowers the interfacial impedance during cycling.

2.3 The lithium deposition behavior and modification mechanism

2.3.1 Lithium deposition behavior

The morphology of Li deposition on the current collectors with various capacities plated at 0.3 mA·cm^{-2} was examined by SEM and *in-situ* optical microscopy to investigate the regulating effect of the modification layer on lithium plating behavior. The initial nucleation of Li on bare Cu is very heterogeneous, and gradually forms some locally stacked particles with a diameter of ~ 3.5 μm (Fig. 5(a1) and Fig. S7(a1) in the ESM). Due to the absence of lithiophlic sites, the nucleation is heterogeneous. Initially, the $LiNO_3$ additive in the electrolyte enables thin protective Li_3N-containing film on the surface of the lithium and repairs any ruptures at the interface, which significantly enhances the ionic conductivity of the SEI. This shifts the reaction rate step of lithium deposition from diffusion control to reaction control, resulting in spherical lithium nucleation [64–66]. By contrast, the nucleation of Li on NC@RGO@Cu (Fig. 5(b1) and Figs. S7(b1)–S7(b5) in the ESM) and Zn@NC@RGO@Cu (Fig. 5(c1) and Figs. S7(c5)–S7(c5) in the ESM) is more uniform, especially on the surface of Zn@NC@RGO@Cu (Fig. 5(c1)). When lithium deposition increases to 1 mAh·cm^{-2}, Li accumulates locally on the surface of copper foil and forms loose Li dendrites with diameter of ~ 2–3 μm (Figs. S7(a2)–S7(a4) in the ESM). Continuous interfacial side reactions and formation of SEI result in increased SEI impedance, which hinders the fast charge transfer and increases cell polarization. The lithium plating changes from reaction control to diffusion control, facilitating the dendrite

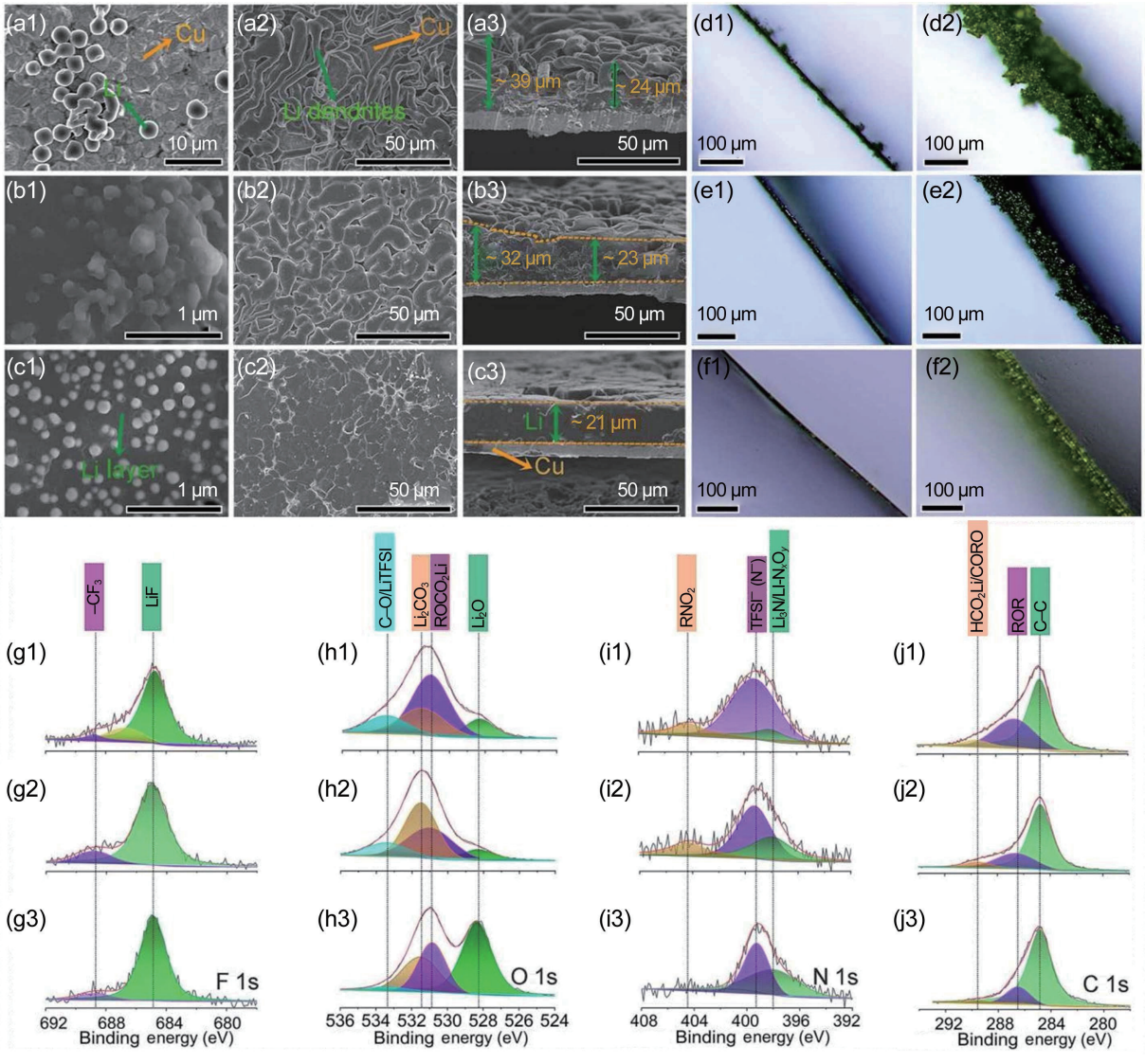

Figure 5 Morphology evolution and *in-situ* optical images for plating various Li amount at 0.3 mA·cm^{-2} of Cu foil, NC@RGO@Cu, and Zn@NC@RGO@Cu electrode in anode half-cells: the top view SEM images of ((a1) and (a2)) Cu foil electrode, ((b1) and (b2)) NC@RGO@Cu electrode, and ((c1) and (c2)) Zn@NC@RGO@Cu electrode with an areal capacity of 0.1 and 4 mAh·cm^{-2} at 0.3 mA·cm^{-2}. The cross-sectional morphology of (a3) Cu foil electrode, (b3) NC@RGO@Cu electrode, and (c3) Zn@NC@RGO@Cu electrode with an areal capacity of 4 mAh·cm^{-2} at 0.3 mA·cm^{-2}. *In-situ* optical microscopy images of the side view for the different electrodes after deposition of ((d1), (e1), and (f1)) 0.1 mAh·cm^{-2} and ((d2), (e2), and (f2)) 4 mAh·cm^{-2} of Li. Deconvoluted XPS spectra, F 1s, O 1s, N 1s, and C 1s in the SEI layer of ((g1), (h1), (i1), and (j1)) Cu foil, ((g2), (h2), (i2), and (j2)) NC@RGO@Cu, and ((g3), (h3), (i3), and (j3)) Zn@NC@RGO@Cu electrode after 30 cycles.

formation [64]. Contrarily, dense Li grows evenly along the radial direction as well as upward in mosaic shape on the surface of NC@RGO@Cu (Figs. S7(b2)–S7(b4) in the ESM) and Zn@NC@RGO@Cu (Figs. S7(c2)–S7(c4) in the ESM). Dendrites on bare Cu continuously grow upward with increasing lithium deposition (Fig. 5(a2) and Fig. S7(a5) in the ESM). A layer of Li dendrites with relatively larger diameter (~ 2.5–6 μm) also forms on NC@RGO@Cu when the deposition amount is larger than 2 mAh·cm^{-2} (Fig. 5(b2) and Fig. S7(b5) in the ESM). However, the Li deposition continues growing uniformly and densely on Zn@NC@RGO@Cu with extra Li clusters appearing on top of the bottom layer at 2 mAh·cm^{-2} (Fig. S7(c5) in the ESM), and there are no Li dendrites even at 4 mAh·cm^{-2} (Fig. 5(c2)). As a result, the Li plating on Cu foil is quite loose and uneven with the thickness of 24–39 μm at 4 mAh·cm^{-2} (Fig. 5(a3)). The deposition morphology on NC@RGO@Cu (Fig. 5(b3)) is slightly improved with the thickness of ~ 23–32 μm. Due to the excellent regulation effect of modification layer, Li forms a much denser and uniform layer (~ 21 μm) on Zn@NC@RGO@Cu (Fig. 5(c3)). The postmortem morphology analysis reveals that Zn@NC@RGO@Cu cell lasts longer and exhibits more uniform morphology even after cell failure (Fig. S8 in the ESM).

The *in-situ* optical microscopy was conducted in the assembled light mirror electrolytic cell (Fig. S9 in the ESM) to track the Li deposition process and observe the morphology changes of lithium in real time. The local accumulation of Li forms rapidly on the bare Cu. With increasing deposition, the Li dendrites grow severely upwards out of control with a final thickness of > 95 μm (Figs. 5(d1) and 5(d2), and Video ESM1). Under the same circumstances, Li spreads uniformly and grows smoothly bottom-up on the modified current collectors, especially on Zn@NC@RGO@Cu. After 3 h (~ 0.9 mAh·cm^{-2}), clusters of Li appear on the NC@RGO@Cu (Video ESM2), and the continuous accumulation of uneven precipitation leads to bulge in some places until the original SEI film is broken. Finally, loose Li dendrites form after 6 h (Figs. 5(e1) and 5(e2)). By contrast, a dense and compact deposition layer is achieved on the Zn@NC@RGO@Cu (Figs. 5(f1) and 5(f2), and Video ESM3). Even after plating 4 mAh·cm^{-2} of Li, the deposition layer is smooth and no dendrite is observed. The deposition thickness is decreased remarkably to ~ 25 μm at the front end of deposition layer, as a result of the regulated Li platting behavior by the modification layer. It should be noted that the growth of lithium is less restrained here in this optical configuration, which is slightly different from that in coin cells with cell pressure. These results prove that the N-doped carbon modified layer NC@RGO can induce the uniform nucleation and deposition of Li to some extent. Additionally, the introduction of atomically dispersed zinc-coordination lithiophilic sites on Zn@NC@RGO can further homogenize the nucleation of Li^+ flux and therefore regulate the Li deposition to achieve dense and uniform platting.

2.3.2 SEI analysis

The chemical composition of the SEI layers was analyzed by XPS. Generally, the contents of Li, N, and F are the highest while those of C and O are the lowest in the SEI on Zn@NC@RGO@Cu (Fig. S10 in the ESM) after 30 cycles. The detailed contents of some key components in the SEI are listed in Table S2 in the ESM. Compared with the SEI on bare Cu, as shown in the F 1s spectra (Figs. 5(g1)–5(g3)) and N 1s spectra (Figs. 5(i1)–5(i3)), the content of LiF (685.0 eV) and Li_3N/Li-N_xO_y (398.1 eV) inorganic matter in the SEI increases significantly from 1.9% and 0.2% on bare Cu to 2.8% and 0.5% on NC@RGO@Cu, and 4.2% and 0.9% on Zn@NC@RGO@Cu, respectively. At the same time, the contents of $ROCO_2Li$ (530.7 eV), HCO_2Li (289.5 eV), $TFSI^-$ (N^-, 399.2 eV), and ROR (286.6 eV) from the decomposition of electrolyte solvent/lithium salts decrease significantly (Figs. 5(h1)–5(h3) and 5(j1)–5(j3)) after the introduction of modification layer, especially in the Zn@NC@RGO@Cu case. The contents of inorganic components in the SEI on NC@RGO@Cu (Li_2CO_3-531.5 eV) and on Zn@NC@RGO@Cu (Li_2O-528.3 eV) are much higher than those on bare Cu (Table S2 in the ESM). The total contents of the main inorganic components in the SEI film on Zn@NC@RGO@Cu (25.2%) are much higher than those in NC@RGO@Cu (19.0%) and Cu (12.4%). LiF, Li_3N, Li_2CO_3, and Li_2O possess high ionic conductivity in the sequence of LiF < Li_2CO_3 < Li_2O < Li_3N to promote ion diffusion, and have high Young's modulus to inhibit the growth of lithium dendrites. Additionally, Li_2O in dense SEI can effectively regulate the stripping and transport of Li^+ due to its extremely low solubility in electrolyte [67, 68]. Therefore, dense SEI rich in inorganic lithium compounds can effectively inhibit the growth of lithium dendrites and reduce interfacial side reactions, which are key factors for Zn@NC@RGO@Cu to achieve stable lithium cycling. Moreover, the postmortem analysis on SEI layer in the cycled electrode after cell failure (Fig. S11 in the ESM) also shows that the surface of Zn@NC@RGO@Cu is still rich in inorganic components, such as LiF, Li_2CO_3, and Li_3N, compared with others. This enables the effective inhibition of Li dendrite growth even after long-term cycling, which is consistent with the above postmortem SEM results.

2.3.3 Density functional theory (DFT) analysis

DFT calculation implemented in the Vienna *ab initio* simulation package (VASP) was used to understand the lithium affinity and charge transfer properties on different current collectors. The adsorption energy E_a was determined by [27, 69]: $E_a = E_{total} - E_{sub} - E_{Li}$, where E_{total}, E_{sub}, and E_{Li} are the total energy of the substrates bound with a Li atom, pristine substrates, and a Li atom, respectively. The structure of adsorbed lithium on the (111) plane of Cu was calculated to be the most stable adsorption structure with an adsorption energy of −2.5 eV (Fig. 6(a1)), which is consistent with the previous reports [40, 70]. The optimal adsorption site and adsorption energy of Li atom on Zn@NC@RGO@Cu are calculated by periodically repeated slabs of pure graphene sheets (PGs) and PGs with Zn-(C/N/O) sites (ZnGs) as a model structure, respectively. When a Li atom is adsorbed on the Cu substrate, there is large charge accumulation between Li and Cu (111) (Fig. 6(b1)), and the electron transfer is faster than the diffusion of lithium ion, leading to the uneven deposition of lithium. As shown in Figs. 6(a2) and 6(b2), charge accumulation still exists between lithium and the PGs with an adsorption energy of −1.45 eV. By contrast, the introduction of heterogeneous Zn-(C/N/O) sites can significantly reduce the charge accumulation. Noteworthy, the results show that the Zn-(C/N/O) site is the most stable site for Li adsorption on ZnGs, and Li atoms preferentially form C-Zn-(N/O)-Li rather than other adsorption structures. The adsorption energy of lithium at the Zn-(C/N/O) configurations (Fig. 6(a3) and Figs. S12(a)–S12(i) in the ESM) on ZnGs is way lower than that on PGs and Cu, indicating a more stable Li adsorption [51]. The adsorption structure in Fig. 6(a3) exhibits low adsorption energy of −3.72 eV. As shown in Fig. 6(b3), there is a charge loss region above Li atom due to the charge transfer from Li to ZnGs, suggesting the lithiophilicity of the Zn-(C/N/O) sites. And the charges remain scattered rather than accumulated after adsorption, which is beneficial to improve the charge transfer kinetics during lithium deposition and facilitate homogeneous Li nucleation and growth. Possible N-Zn-O_2 sites possess lower lithium adsorption energy (−3.91 eV) (Figs. S12(d) and S12(e) in the ESM), however, the corresponding charge

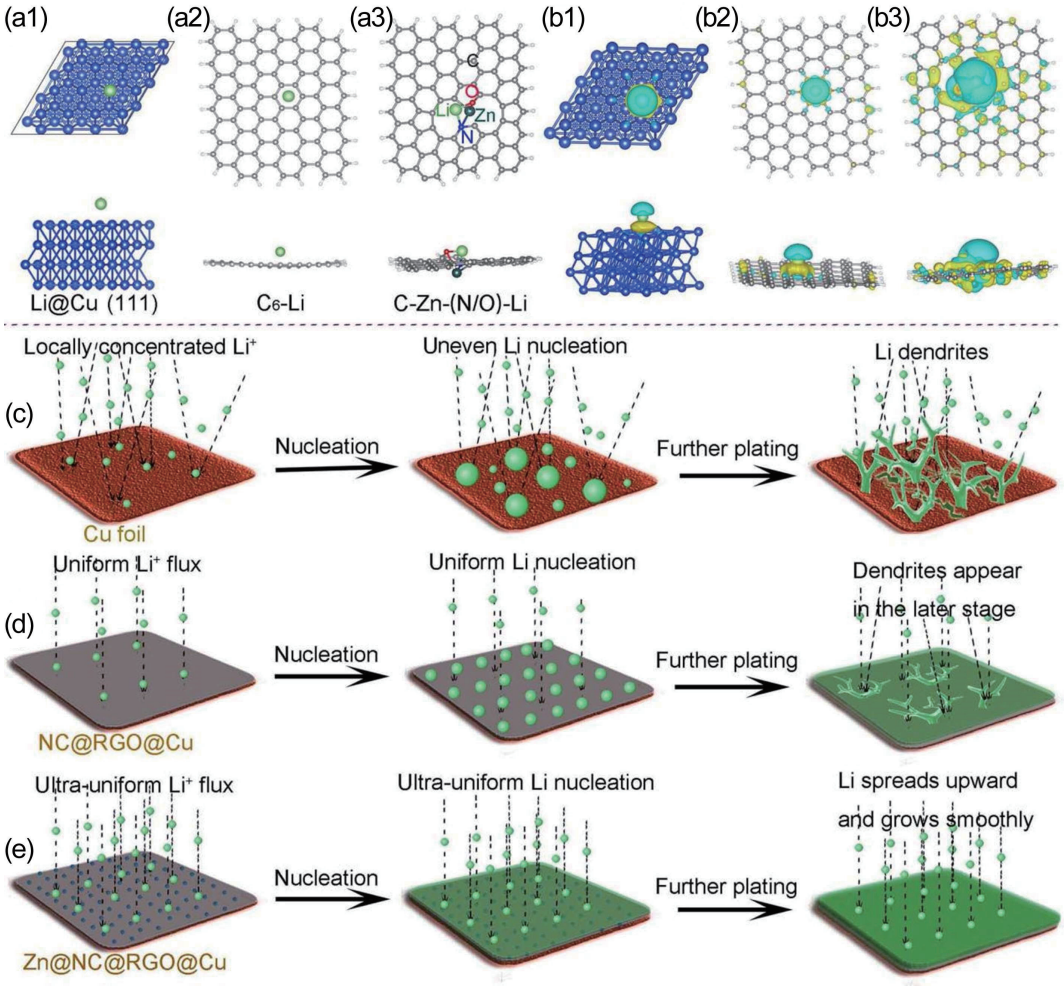

Figure 6 DFT calculations and schematic diagrams of lithium deposition at different electrodes. (a1)–(a3) Adsorption energy of the optimized interaction geometry of a Li atom with Cu (111), PGs, and single atom Zn doped isolated ZnGs, respectively, (top view and side view). (b1)–(b3) Corresponding charge density differences of the optimized interaction geometry of a Li atom with Cu (111), PGs, and ZnGs, respectively, (top view and side view). (The isosurface value is set to 0.002 e·Å^{-3}. Light blue and yellow represent charge loss and accumulation, respectively). (c)–(e) The schematic diagrams of lithium deposition at Cu foil, NC@RGO@Cu, and Zn@NC@RGO@Cu electrode.

transfer is obviously not as good as Zn-(C/N/O) sites (Figs. S12(f) and S12(g) in the ESM). The process of lithium nucleation and growth is affected by electric field force, Li^+ concentration gradient, and the electrostatic interaction between Li^+ and electronegative sites on the substrates. Electrostatic interaction plays a key role to regulate the lithium plating morphology, since charge transfer will occur immediately once lithium ions are adsorbed. The single atomic Zn-(C/N/O) functional sites can facilitate homogeneous and stable adsorption of Li, which will greatly increase the Li affinity of the modification layer, reduce the Li deposition barrier, and effectively regulate the uniform nucleation and stable deposition of Li.

Based on the electrochemical characterization and DFT calculation, Figs. 6(c)–6(e) show the schematic diagrams of lithium deposition at Cu foil (Fig. 6(c)), NC@RGO@Cu (Fig. 6(d)), and Zn@NC@RGO@Cu current collectors (Fig. 6(e)). Locally concentrated Li^+ flux and uneven lithium nuclei are easily formed on the lithiophobic surface of bare Cu due to the high lithium nucleation overpotential [70–73], resulting in the uncontrollable and violent growth of dendrites and decreased cycle stability. Relatively uniform Li^+ flux and nucleation sites are formed on the NC@RGO@Cu due to the introduction of modification layer with N/O heteroatoms. However, the improvement of lithium affinity is limited, and certain amounts of dendrites will inevitably appear with large amounts of lithium plated. The as-prepared Zn@NC@RGO@Cu current collector has obvious advantages in stabilizing Li plating/stripping. Firstly, the thickness of the modified layer is only about 600 nm, only 6.67% of the thickness of Cu foil, and the relative mass can be ignored, which is substantial for the improvement of volumetric and gravimetric energy density for AFLMBs. Secondly, the *in-situ* synthesis approach using GO and Zn-PDA ensures good contact between the modification layer and the Cu substrate, which would enable high conductivity and fast charge transfer. Thirdly, the surface of the modified layer is rich in Zn-(C/N/O) lithiophilic sites, which can not only facilitate smooth and dense SEI formation, but also homogenize the Li^+ flux, so as to improve the uniformity of lithium deposition. Most importantly, the distribution of monatomic Zn sites in carbon medium is super uniform and has excellent lithium affinity, which can significantly reduce the nucleation barrier of lithium and promote the ultra-uniform nucleation. As a result, a layer of densely ultra-thin lithium is efficiently formed on the lithium nuclei, spreads upward, and grows smoothly.

2.4 Electrochemical performance of anode-free lithium metal battery

In order to further demonstrate the potential application of Zn@NC@RGO@Cu in AFLMBs, full cells were assembled with current collectors paired with commercial $LiFePO_4$ (LFP) cathode in areal capacity of ~ 1.6 mAh·cm^{-2} as shown in Figs. 7(a)–7(c). Figure 7(d) shows the cycling behavior of LFP||Cu,

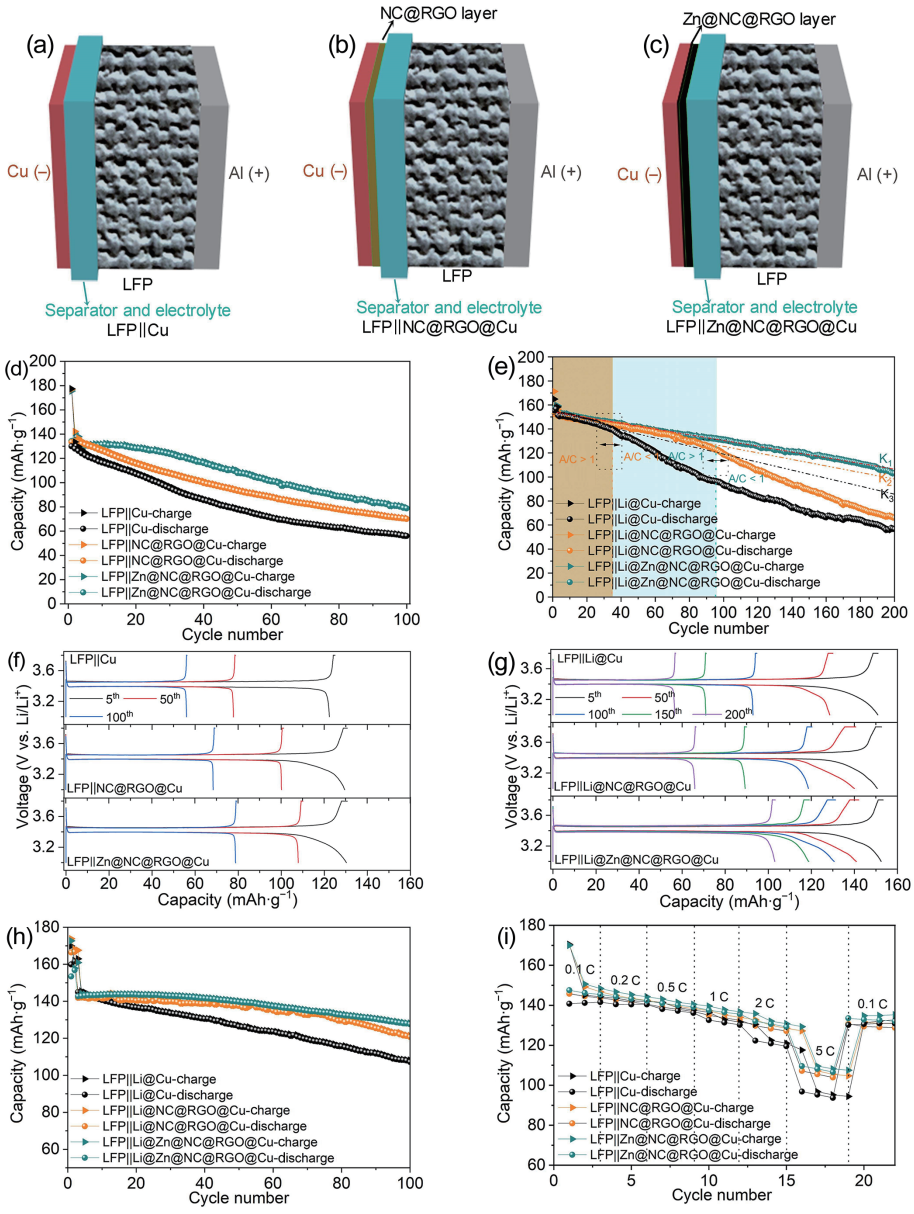

Figure 7 The demonstration of LFP based AFLMBs. Schematic diagrams of assembled lithium metal battery system of (a) LFP||Cu, (b) LFP||NC@RGO@Cu, and (c) LFP||Zn@NC@RGO@Cu, respectively. (d) Cycling performance of LFP||Cu, LFP||NC@RGO@Cu, and LFP||Zn@NC@RGO@Cu coin cells at the charge/discharge rate of 0.2 C/0.3 C. (e) Cycling performance of LFP||Li@Cu, LFP||Li@NC@RGO@Cu, and LFP||Li@Zn@NC@RGO@Cu coin cells at the charge/discharge rate of 0.2 C/0.3 C. (f) Voltage curves of LFP||Cu, LFP||NC@RGO@Cu, and LFP||Zn@NC@RGO@Cu full cells at the 5th, 50th, and 100th cycle. (g) Voltage curves of LFP||Li@Cu, LFP||Li@NC@RGO@Cu, and LFP||Li@Zn@NC@RGO@Cu full cells at the 5th, 50th, 100th, 150th, and 200th cycle. (h) Long cycle performance of LFP||Li@Cu, LFP||Li@NC@RGO@Cu, and LFP||Li@Zn@NC@RGO@Cu coin cells with the charge/discharge rate of 0.6 C/1.0 C at the temperature of 35 °C. (i) Electrochemical performance of LFP||Cu, LFP||NC@RGO@Cu, and LFP||Zn@NC@RGO@Cu at different C-rates (35 °C).

LFP||NC@RGO@Cu, and LFP||Zn@NC@RGO@Cu full cells between the potential window of 3.0–3.8 V with the charge/discharge rate of 0.2 C/0.3 C in 1 M LiTFSI (DOL:DME = 1:1) ether-based electrolyte at the temperature of 25 °C. Compared to the reference samples, LFP||Zn@NC@RGO@Cu exhibits higher capacity retention as well as higher reversible capacity. As shown in Fig. S13(a) in the ESM, the initial CE (ICE) and ACE of LFP||Zn@NC@RGO@Cu cell are 76.2% and 99.51%, which are much higher than those of LFP||NC@RGO@Cu cell (75.5% and 99.37%) and LFP||Cu cell (73.3% and 99.19%). The improved ICE and ACE demonstrate greatly reduced interfacial side reactions between the anode and the electrolyte, which are related to the homogeneous deposition of lithium induced by Zn@NC@RGO@Cu and the formation of more robust and stable SEI film on the surface of Zn@NC@RGO@Cu, as revealed above by lithium deposition behavior above in Section 2.3. Therefore, the capacity retention ratio (CRR) of 44.4%, 53.3%, and 61.4% are retained after 100 cycles in the LFP||Cu, LFP||NC@RGO@Cu, and LFP||Zn@NC@RGO@Cu coin cells, respectively. The voltage curves in Fig. 7(f) also demonstrate much slower capacity decay in LFP||Zn@NC@RGO@Cu. It turns out that the modified layer with ultra-uniformly dispersed single atomic Zn lithiophilic sites in carbon medium can effectively improve the cycle stability of the AFLMB system.

1 mAh·cm^{-2} of lithium was pre-deposited on the current collector as a supplementary lithium source and paired with LFP in full cell configuration to further understand the fading mechanism in the full cells. Since there is excess active lithium on the anode current collectors, the capacity ratio of anode to cathode (A/C) is greater than 1 initially. The excess Li will compensate for the loss of active Li caused by the formation of dead lithium and the side reactions between Li and electrolyte with cycling, resulting in a decreased A/C value and elevated capacity degradation speed. As shown in Fig. 7(e), all the cycling profiles show three stages of

capacity fade. In the first stage, A/C > 1, there is excess lithium due to the predeposited lithium and all battery systems exhibit a gentle attenuation slope, among which the capacity decay of LFP||Li@Zn@NC@RGO@Cu coin cell is the smallest and lasts until 200 cycles without sudden increase of attenuation slope. With the progress of the cycle, the active lithium is gradually consumed to reach the stage of A/C < 1, and the cell begins to decay rapidly. There is a sudden increase of the decay slope appearing at the 96th cycle in LFP||Li@NC@RGO@Cu and at the 35th cycle in LFP||Li@Cu system, suggesting the occurrence of A/C < 1 due to the continuous consumption of active lithium. Compared with NC@RGO@Cu and Cu, Zn@NC@RGO@Cu can still effectively stabilize lithium deposition at a large amount of lithium deposition amount of 4 mAh·cm^{-2} (greater than the total amount of lithium in the battery system). At the same time, the sturdier SEI film on the surface of Li@Zn@NC@RGO@Cu also avoids the formation of a large number of dead lithium, improves the cycle efficiency, and effectively delays the emergence of stage with A/C < 1. As shown in Fig. S13(b) in the ESM, the ICE, ACE, and CRR are increased to 99.83%, 95.42%, and 85.1% in the LFP||Li@Zn@NC@RGO@Cu full cell due to the supplement of lithium source. In contrast, the ICE, ACE, and CRR of the LFP||Li@NC@RGO@Cu and Li LFP||Li@Cu cell are 99.76%, 89.04%, and 78.6%, and 99.50%, 94.11%, and 61.1%, respectively.

The voltage curves in Fig. 7(g) show that the capacity and cycling stability are greatly improved in the LFP||Li@Zn@NC@RGO@Cu system with discharge capacity of 152.4, 140.8, 130.6, 118.8, and 103.0 mAh·g^{-1} at the 5th, 50th, 100th, 150th, and 200th cycle, which is obviously much better than that in the LFP||Li@NC@RGO@Cu (150.6, 139.9, 118.5, 89.3, and 65.9 mAh·g^{-1}) and LFP||Li@Cu (150.8, 128.5, 92.8, 71.0, and 56.4 mAh·g^{-1}) systems. The energy density of LFP||Li@Zn@NC@RGO@Cu full cell is ~ 518 Wh·kg^{-1} (calculated based on the cathode and predeposited lithium). The energy density of the LFP||Li@Zn@NC@RGO@Cu battery pack is anticipated to be increased by ~ 19.1% (single-side coated cathode) compared to the LFP||graphite battery pack, and theoretically, it can be significantly increased by ~ 22.6% when using a double-side coated cathode. The performance of the battery at relatively high temperature and high rate was also studied. As shown in Fig. 7(h), the CRRs (ACEs) of 74.5% (~ 99.71%), 85.5% (~ 99.84%), and 89.7% (~ 99.89%) are retained after 100 cycles in the LFP||Li@Cu, LFP||Li@NC@RGO@Cu, and LFP||Li@Zn@NC@RGO@Cu full cells at the charge/discharge rate of 0.6 C/1.0 C at 35 °C. As for the rate capability, the capacity retention of LFP||Cu, LFP||NC@RGO@Cu, and LFP||Zn@NC@RGO@Cu cells are 68.8%, 73.5%, and 74.3%, respectively, when cycled from 0.1 to 5 C (Fig. 7(i)). The increased rate capability of LFP||Zn@NC@RGO@Cu at high rates is due to the effective regulation of lithium plating/stripping by the lithiophilic modification layer, which leads to more uniform SEI and less dead lithium/inactive side products. The interfacial resistance is much lower, as demonstrated above in Fig. 4. Thus the interfacial charge transfer kinetics during cycling is facilitated and the cycle stability is improved, especially at high rates. The performance of the Zn@NC@RGO@Cu current collector for AFLMB is compared with the state-of-the-art AFLMBs reported in literatures in Table S3 in the ESM. Zn@NC@RGO@Cu shows superior cycle efficiency and stability among the AFLMBs system, which shows that the single atomic Zn dispersed in N/O co-doped amorphous carbon medium modified layer is quite effective in inducing, regulating, and stabilizing lithium plating/stripping.

3 Conclusions

In summary, atomically dispersed lithiophilic zinc sites together with N/O co-doped amorphous carbon medium were introduced on Cu current collector through the assistance of GO and PDA by an *in-situ* induced ion coordination chemistry strategy, which ensures the conductivity, flexibility, and robustness of the modified layer in the Zn@NC@RGO@Cu. XAS combined with HAADF-STEM analysis proved the single atomic state of the zinc sites surrounded by N and O with a coordination number of ~ 3. *In-situ* and *ex-situ* measurements combined with first principle calculations demonstrate that the introduction of lithiophilic Zn-(C/N/O) single atomic sites greatly enhance the adsorption behavior of lithium at the current collector, which is a key to the dendrites suppression and uniform lithium deposition. Uniform lithium nucleation and deposition enable stable Li plating/stripping and elevated Coulombic efficiency of 98.95% in anode-free Li||Cu coin cell after > 850 cycles. As a result, high capacity retention of 61.4% is successfully achieved in the LFP||Zn@NC@RGO@Cu anode-free lithium metal battery after 100 cycles, and the capacity retention is further improved to 89.7% after 100 cycles in LFP||Li@Zn@NC@RGO@Cu. These findings not only provide a feasible approach to improve the cyclability of anode-free lithium metal battery by introducing single atomic lithiophilic sites on Cu current collector, but also shed light on the understanding of SEI evolution, interfacial stabilization, and Li protection strategy in advanced practical Li metal-based battery systems with higher energy density and high security in the future.

Acknowledgements

This work was supported by Department of Science and Technology of Guangdong Province (No. 211233812024), Guangdong Basic and Applied Basic Research Foundation (No. 2021A1515110871), Shenzhen Science and Technology Program (Nos. JCYJ20220818101007016 and JCYJ20210324140804013), and Tsinghua Shenzhen International Graduate School (No. QD2021005N).

Electronic Supplementary Material: Supplementary material (experimental and methods, supporting figures, supporting tables, and references) is available in the online version of this article at https://doi.org/10.1007/s12274-023-5795-7.

References

[1] Brandt, L. R.; Marie, J. J.; Moxham, T.; Förstermann, D. P.; Salvati, E.; Besnard, C.; Papadaki, C.; Wang, Z. F.; Bruce, P. G.; Korsunsky, A. M. Synchrotron X-ray quantitative evaluation of transient deformation and damage phenomena in a single nickel-rich cathode particle. *Energy Environ. Sci.* **2020**, *13*, 3556–3566.

[2] Lv, Y.; Huang, S. F.; Zhao, Y. F.; Roy, S.; Lu, X. G.; Hou, Y. L.; Zhang, J. J. A review of nickel-rich layered oxide cathodes: Synthetic strategies, structural characteristics, failure mechanism, improvement approaches and prospects. *Appl. Energy* **2022**, *305*, 117849.

[3] Liu, Q.; Su, X.; Lei, D.; Qin, Y.; Wen, J. G.; Guo, F. M.; Wu, Y. A.; Rong, Y. C.; Kou, R. H.; Xiao, X. H. et al. Approaching the capacity limit of lithium cobalt oxide in lithium ion batteries via lanthanum and aluminium doping. *Nat. Energy* **2018**, *3*, 936–943.

[4] Li, P.; Hwang, J. Y.; Sun, Y. K. Nano/microstructured silicon-graphite composite anode for high-energy-density Li-ion battery. *ACS Nano* **2019**, *13*, 2624–2633.

[5] Zhao, S. Q.; Guo, Z. Q.; Yan, K.; Wan, S. W.; He, F. R.; Sun, B.; Wang, G. X. Towards high-energy-density lithium-ion batteries: Strategies for developing high-capacity lithium-rich cathode materials. *Energy Storage Mater.* **2021**, *34*, 716–734.

[6] Zhang, H.; Yang, Y.; Ren, D. S.; Wang, L.; He, X. M. Graphite as anode materials: Fundamental mechanism, recent progress and advances. *Energy Storage Mater.* **2021**, *36*, 147–170.

[7] Yi, J. S.; Chen, J. H.; Yang, Z.; Dai, Y.; Li, W. M.; Cui, J.; Ciucci, F.; Lu, Z. H.; Yang, C. L. Facile patterning of laser-induced graphene with tailored Li nucleation kinetics for stable lithium-metal batteries. *Adv. Energy Mater.* **2019**, *9*, 1901796.
[8] Schmuch, R.; Wagner, R.; Hörpel, G.; Placke, T.; Winter, M. Performance and cost of materials for lithium-based rechargeable automotive batteries. *Nat. Energy* **2018**, *3*, 267–278.
[9] Han, B.; Xu, D. W.; Chi, S. S.; He, D. S.; Zhang, Z.; Du, L. L.; Gu, M.; Wang, C. Y.; Meng, H.; Xu, K. et al. 500 $Wh{\cdot}kg^{-1}$ class Li metal battery enabled by a self-organized core–shell composite anode. *Adv. Mater.* **2020**, *32*, 2004793.
[10] Wu, F. L.; Fang, S.; Kuenzel, M.; Mullaliu, A.; Kim, J. K.; Gao, X. P.; Diemant, T.; Kim, G. T.; Passerini, S. Dual-anion ionic liquid electrolyte enables stable Ni-rich cathodes in lithium-metal batteries. *Joule* **2021**, *5*, 2177–2194.
[11] Lin, D. C.; Liu, Y. Y.; Cui, Y. Reviving the lithium metal anode for high-energy batteries. *Nat. Nanotechnol.* **2017**, *12*, 194–206.
[12] Chen, X. R.; Zhao, B. C.; Yan, C.; Zhang, Q. Review on Li deposition in working batteries: From nucleation to early growth. *Adv. Mater.* **2021**, *33*, 2004128.
[13] Wen, Z. P.; Peng, Y. Y.; Cong, J. L.; Hua, H. M.; Lin, Y. X.; Xiong, J.; Zeng, J.; Zhao, J. B. A stable artificial protective layer for high capacity dendrite-free lithium metal anode. *Nano Res.* **2019**, *12*, 2535–2542.
[14] Foroozan, T.; Soto, F. A.; Yurkiv, V.; Sharifi-Asl, S.; Deivanayagam, R.; Huang, Z. N.; Rojaee, R.; Mashayek, F.; Balbuena, P. B.; Shahbazian-Yassar, R. Synergistic effect of graphene oxide for impeding the dendritic plating of Li. *Adv. Energy Mater.* **2018**, *28*, 1705917.
[15] Zhao, C. Z.; Chen, P. Y.; Zhang, R.; Chen, X.; Li, B. Q.; Zhang, X. Q.; Cheng, X. B.; Zhang, Q. An ion redistributor for dendrite-free lithium metal anodes. *Sci. Adv.* **2018**, *4*, eaat3446.
[16] Li, G. C.; Duan, X. R.; Liu, X. T.; Zhan, R. M.; Wang, X. C.; Du, J. M.; Chen, Z. H.; Li, Y. J.; Cai, Z.; Shen, Y. et al. Locking active Li metal through localized redistribution of fluoride enabling stable Li-metal batteries. *Adv. Mater.* **2023**, *35*, 2207310.
[17] Jiang, Z. P.; Zeng, Z. Q.; Liang, X. M.; Yang, L.; Hu, W.; Zhang, C.; Han, Z. L.; Feng, J. W.; Xie, J. Fluorobenzene, a low-density, economical, and bifunctional hydrocarbon cosolvent for practical lithium metal batteries. *Adv. Funct. Mater.* **2021**, *31*, 2005991.
[18] Zhang, H.; Zeng, Z. Q.; He, R. J.; Wu, Y. K.; Hu, W.; Lei, S.; Liu, M. C.; Cheng, S. J.; Xie, J. 1,3,5-Trifluorobenzene and fluorobenzene co-assisted electrolyte with thermodynamic and interfacial stabilities for high-voltage lithium metal battery. *Energy Storage Mater.* **2022**, *48*, 393–402.
[19] Zhang, H.; Zeng, Z. Q.; Ma, F. F.; Wu, Q.; Wang, X. L.; Cheng, S. J.; Xie, J. Cyclopentylmethyl ether, a non-fluorinated, weakly solvating and wide temperature solvent for high-performance lithium metal battery. *Angew. Chem., Int. Ed.*, in press, https://doi.org/10.1002/anie.202300771.
[20] Genovese, M.; Louli, A. J.; Weber, R.; Hames, S.; Dahn, J. R. Measuring the Coulombic efficiency of lithium metal cycling in anode-free lithium metal batteries. *J. Electrochem. Soc.* **2018**, *165*, A3321–A3325.
[21] Gu, Y.; Xu, H. Y.; Zhang, X. G.; Wang, W. W.; He, J. W.; Tang, S.; Yan, J. W.; Wu, D. Y.; Zheng, M. S.; Dong, Q. F. et al. Lithiophilic faceted Cu (100) surfaces: High utilization of host surface and cavities for lithium metal anodes. *Angew. Chem., Int. Ed.* **2019**, *58*, 3092–3096.
[22] Li, Y. Z.; Li, Y. B.; Pei, A.; Yan, K.; Sun, Y. M.; Wu, C. L.; Joubert, L. M.; Chin, R.; Koh, A. L.; Yu, Y. et al. Atomic structure of sensitive battery materials and interfaces revealed by cryo-electron microscopy. *Science* **2017**, *358*, 506–510.
[23] Lin, L. D.; Suo, L. M.; Hu, Y. S.; Li, H.; Huang, X. J.; Chen, L. Q. Epitaxial induced plating current-collector lasting lifespan of anode-free lithium metal battery. *Adv. Energy Mater.* **2021**, *11*, 2003709.
[24] Chen, W. Y.; Salvatierra, R. V.; Ren, M. Q.; Chen, J. H.; Stanford, M. G.; Tour, J. M. Laser-induced silicon oxide for anode-free lithium metal batteries. *Adv. Mater.* **2020**, *32*, 2002850.
[25] Zhang, C.; Lv, W.; Zhou, G. M.; Huang, Z. J.; Zhang, Y. B.; Lyu, R.; Wu, H. L.; Yun, Q. B.; Kang, F. Y.; Yang, Q. H. Vertically aligned lithiophilic CuO nanosheets on a Cu collector to stabilize lithium deposition for lithium metal batteries. *Adv. Energy Mater.* **2018**, *8*, 1703404.
[26] Assegie, A. A.; Cheng, J. H.; Kuo, L. M.; Su, W. N.; Hwang, B. J. Polyethylene oxide film coating enhances lithium cycling efficiency of an anode-free lithium-metal battery. *Nanoscale* **2018**, *10*, 6125–6138.
[27] Zhang, R.; Wen, S. W.; Wang, N.; Qin, K. Q.; Liu, E. Z.; Shi, C. S.; Zhao, N. Q. N-doped graphene modified 3D porous Cu current collector toward microscale homogeneous Li deposition for Li metal anodes. *Adv. Energy Mater.* **2018**, *8*, 1800914.
[28] Wang, X. C.; He, Y. F.; Tu, S. B.; Fu, L.; Chen, Z. H.; Liu, S. Y.; Cai, Z.; Wang, L.; He, X. M.; Sun, Y. M. Li plating on alloy with superior electro-mechanical stability for high energy density anode-free batteries. *Energy Storage Mater.* **2022**, *49*, 135–143.
[29] Zhou, S. H.; Huang, P.; Xiong, T. Z.; Yang, F.; Yang, H.; Huang, Y. C.; Li, D.; Deng, J. Q.; Balogun, M. S. Sub-thick electrodes with enhanced transport kinetics via *in situ* epitaxial heterogeneous interfaces for high areal-capacity lithium ion batteries. *Small* **2021**, *17*, 2100778.
[30] Yang, H.; Xiong, T. Z.; Zhu, Z. X.; Xiao, R.; Yao, X. C.; Huang, Y. C.; Balogun, M. S. Deciphering the lithium storage chemistry in flexible carbon fiber-based self-supportive electrodes. *Carbon Energy* **2022**, *4*, 820–832.
[31] Chen, X.; Chen, X. R.; Hou, T. Z.; Li, B. Q.; Cheng, X. B.; Zhang, R.; Zhang, Q. Lithiophilicity chemistry of heteroatom-doped carbon to guide uniform lithium nucleation in lithium metal anodes. *Sci. Adv.* **2019**, *5*, eaau7728.
[32] Wang, Y. L.; Shen, Y. B.; Du, Z. L.; Zhang, X. F.; Wang, K.; Zhang, H. Y.; Kang, T.; Guo, F.; Liu, C. H.; Wu, X. D. et al. A lithium-carbon nanotube composite for stable lithium anodes. *J. Mater. Chem. A* **2017**, *5*, 23434–23439.
[33] Liu, L.; Yin, Y. X.; Li, J. Y.; Wang, S. H.; Guo, Y. G.; Wan, L. J. Uniform lithium nucleation/growth induced by lightweight nitrogen-doped graphitic carbon foams for high-performance lithium metal anodes. *Adv. Mater.* **2018**, *30*, 1706216.
[34] Liu, S.; Wang, A. X.; Li, Q. Q.; Wu, J. S.; Chiou, K.; Huang, J. X.; Luo, J. Y. Crumpled graphene balls stabilized dendrite-free lithium metal anodes. *Joule* **2018**, *2*, 184–193.
[35] Ma, Y.; Gu, Y. T.; He, Y.; Wei, L.; Lian, Y. B.; Pan, W. Y.; Li, X. J.; Su, Y. H.; Peng, Y.; Deng, Z. et al. Fast-charging and dendrite-free lithium metal anode enabled by partial lithiation of graphene aerogel. *Nano Res.* **2022**, *15*, 9792–9799.
[36] Ye, W. B.; Pei, F.; Lan, X. N.; Cheng, Y.; Fang, X. L.; Zhang, Q. B.; Zheng, N. F.; Peng, D. L.; Wang, M. S. Stable nano-encapsulation of lithium through seed-free selective deposition for high-performance Li battery anodes. *Adv. Energy Mater.* **2020**, *10*, 1902956.
[37] Wang, T. S.; Liu, X. B.; Zhao, X. D.; He, P. G.; Nan, C. W.; Fan, L. Z. Regulating uniform Li plating/stripping via dual-conductive metal-organic frameworks for high-rate lithium metal batteries. *Adv. Funct. Mater.* **2020**, *30*, 2000786.
[38] Zhang, D.; Dai, A.; Fan, B. F.; Li, Y. G.; Shen, K.; Xiao, T.; Hou, G. Y.; Cao, H. Z.; Tao, X. Y.; Tang, Y. P. Three-dimensional ordered macro/mesoporous Cu/Zn as a lithiophilic current collector for dendrite-free lithium metal anode. *ACS Appl. Mater. Interfaces* **2020**, *12*, 31542–31551.
[39] Yang, C. P.; Yao, Y. G.; He, S. M.; Xie, H.; Hitz, E.; Hu, L. B. Ultrafine silver nanoparticles for seeded lithium deposition toward stable lithium metal anode. *Adv. Mater.* **2017**, *29*, 1702714.
[40] Fang, Y. J.; Zhang, S. L.; Wu, Z. P.; Luan, D. Y.; Lou, X. W. A highly stable lithium metal anode enabled by Ag nanoparticle-embedded nitrogen-doped carbon macroporous fibers. *Sci. Adv.* **2021**, *7*, eabg3626.
[41] Fang, Y. J.; Zeng, Y. X.; Jin, Q.; Lu, X. F.; Luan, D. Y.; Zhang, X. T.; Lou, X. W. Nitrogen-doped amorphous Zn-carbon multichannel fibers for stable lithium metal anodes. *Angew. Chem., Int. Ed.* **2021**, *60*, 8515–8520.
[42] Wu, H. Q.; Ang, J. M.; Kong, J. H.; Zhao, C. Y.; Du, Y. H.; Lu, X. H. One-pot synthesis of polydopamine-Zn complex antifouling coatings on membranes for ultrafiltration under harsh conditions. *RSC Adv.* **2016**, *6*, 103390–103398.

[43] Wilker, J. J. The iron-fortified adhesive system of marine mussels. *Angew. Chem., Int. Ed.* **2010**, *49*, 8076–8078.
[44] Sever, M. J.; Weisser, J. T.; Monahan, J.; Srinivasan, S.; Wilker, J. J. Metal-mediated cross-linking in the generation of a marine-mussel adhesive. *Angew. Chem., Int. Ed.* **2004**, *43*, 448–450.
[45] Sun, J. J.; Cheng, Y.; Zhang, H. H.; Yan, X. L.; Sun, Z. F.; Ye, W. B.; Li, W. Q.; Zhang, M. Y.; Gao, H. W.; Han, J. J. et al. Enhanced cyclability of lithium metal anodes enabled by anti-aggregation of lithiophilic seeds. *Nano Lett.* **2022**, *22*, 5874–5882.
[46] Wei, N.; Jiang, Y. Y.; Ying, Y.; Guo, X. Y.; Wu, Y. P.; Wen, Y.; Yang, H. F. Facile construction of a polydopamine-based hydrophobic surface for protection of metals against corrosion. *RSC Adv.* **2017**, *7*, 11528–11536.
[47] Chi, S. S.; Wang, Q. R.; Han, B.; Luo, C.; Jiang, Y. D.; Wang, J.; Wang, C. Y.; Yu, Y.; Deng, Y. H. Lithiophilic Zn sites in porous CuZn alloy induced uniform Li nucleation and dendrite-free Li metal deposition. *Nano Lett.* **2020**, *20*, 2724–2732.
[48] Neidhardt, J.; Hultman, L.; Czigány, Z. Correlated high resolution transmission electron microscopy and X-ray photoelectron spectroscopy studies of structured CN_x ($0 < x < 0.25$) thin solid films. *Carbon* **2004**, *42*, 2729–2734.
[49] Czigány, Z.; Hultman, L. Interpretation of electron diffraction patterns from amorphous and fullerene-like carbon allotropes. *Ultramicroscopy* **2010**, *110*, 815–819.
[50] Liu, B.; Yang, C. M.; Liu, Z. W.; Lai, C. S. N-doped graphene with low intrinsic defect densities via a solid source doping technique. *Nanomaterials* **2017**, *7*, 302.
[51] Song, P.; Luo, M.; Liu, X. Z.; Xing, W.; Xu, W. L.; Jiang, Z.; Gu, L. Zn single atom catalyst for highly efficient oxygen reduction reaction. *Adv. Funct. Mater.* **2017**, *27*, 1700802.
[52] Huang, S. F.; Li, Z. P.; Wang, B.; Zhang, J. J.; Peng, Z. Q.; Qi, R. J.; Wang, J.; Zhao, Y. F. N-doping and defective nanographitic domain coupled hard carbon nanoshells for high performance lithium/sodium storage. *Adv. Funct. Mater.* **2018**, *28*, 1706294.
[53] Camacho-Bunquin, J.; Aich, P.; Ferrandon, M.; "Bean" Getsoian, A.; Das, U.; Dogan, F.; Curtiss, L. A.; Miller, J. T.; Marshall, C. L.; Hock, A. S. et al. Single-site zinc on silica catalysts for propylene hydrogenation and propane dehydrogenation: Synthesis and reactivity evaluation using an integrated atomic layer deposition-catalysis instrument. *J. Catal.* **2017**, *345*, 170–182.
[54] Xu, B. L.; Wang, H.; Wang, W. W.; Gao, L. Z.; Li, S. S.; Pan, X. T.; Wang, H. Y.; Yang, H. L.; Meng, X. Q.; Wu, Q. W. et al. A single-atom nanozyme for wound disinfection applications. *Angew. Chem.* **2019**, *131*, 4965–4970.
[55] Wang, J. Y.; Guan, Y. J.; Yu, X. G.; Cao, Y. Z.; Chen, J. Z.; Wang, Y. L.; Hu, B.; Jing, H. W. Photoelectrocatalytic reduction of CO_2 to paraffin using p–n heterojunctions. *iScience* **2020**, *23*, 100768.
[56] Yan, K.; Lu, Z. D.; Lee, H. W.; Xiong, F.; Hsu, P. C.; Li, Y. Z.; Zhao, J.; Chu, S.; Cui, Y. Selective deposition and stable encapsulation of lithium through heterogeneous seeded growth. *Nat. Energy* **2016**, *1*, 16010.
[57] Zhang, R.; Chen, X. R.; Chen, X.; Cheng, X. B.; Zhang, X. Q.; Yan, C.; Zhang, Q. Lithiophilic sites in doped graphene guide uniform lithium nucleation for dendrite-free lithium metal anodes. *Angew. Chem.* **2017**, *129*, 7872–7876.
[58] Guan, X. Z.; Wang, A. X.; Liu, S.; Li, G. J.; Liang, F.; Yang, Y. W.; Liu, X. J.; Luo, J. Y. Controlling nucleation in lithium metal anodes. *Small* **2018**, *14*, 1801423.
[59] Nai, J. W.; Zhao, X. Y.; Yuan, H. D.; Tao, X. Y.; Guo, L. Amorphous carbon-based materials as platform for advanced high-performance anodes in lithium secondary batteries. *Nano Res.* **2021**, *14*, 2053–2066.
[60] Shi, P.; Li, T.; Zhang, R.; Shen, X.; Cheng, X. B.; Xu, R.; Huang, J. Q.; Chen, X. R.; Liu, H.; Zhang, Q. Lithiophilic LiC_6 layers on carbon hosts enabling stable Li metal anode in working batteries. *Adv. Mater.* **2019**, *31*, 1807131.
[61] Xiang, Y. X.; Tao, M. M.; Zhong, G. M.; Liang, Z. T.; Zheng, G. R.; Huang, X.; Liu, X. S.; Jin, Y. T.; Xu, N. B.; Armand, M. et al. Quantitatively analyzing the failure processes of rechargeable Li metal batteries. *Sci. Adv.* **2021**, *7*, eabj3423.
[62] Liu, F.; Xu, R.; Wu, Y. C.; Boyle, D. T.; Yang, A. K.; Xu, J. W.; Zhu, Y. Y.; Ye, Y. S.; Yu, Z. A.; Zhang, Z. W. et al. Dynamic spatial progression of isolated lithium during battery operations. *Nature* **2021**, *600*, 659–663.
[63] Rosso, M.; Brissot, C.; Teyssot, A.; Dollé, M.; Sannier, L.; Tarascon, J. M.; Bouchet, R.; Lascaud, S. Dendrite short-circuit and fuse effect on Li/polymer/Li cells. *Electrochim. Acta* **2006**, *51*, 5334–5340.
[64] Chen, X. R.; Yao, Y. X.; Yan, C.; Zhang, R.; Cheng, X. B.; Zhang, Q. A diffusion-reaction competition mechanism to tailor lithium deposition for lithium-metal batteries. *Angew. Chem., Int. Ed.* **2020**, *59*, 7743–7747.
[65] Liu, Q. Q.; Xu, Y. F.; Wang, J. H.; Zhao, B.; Li, Z. J.; Wu, H. B. Sustained-release nanocapsules enable long-lasting stabilization of Li anode for practical Li-metal batteries. *Nano-Micro Lett.* **2020**, *12*, 176.
[66] Liu, S. F.; Ji, X.; Piao, N.; Chen, J.; Eidson, N.; Xu, J. J.; Wang, P. F.; Chen, L.; Zhang, J. X.; Deng, T. et al. An inorganic-rich solid electrolyte interphase for advanced lithium-metal batteries in carbonate electrolytes. *Angew. Chem., Int. Ed.* **2021**, *60*, 3661–3671.
[67] Tan, J.; Matz, J.; Dong, P.; Shen, J. F.; Ye, M. X. A growing appreciation for the role of LiF in the solid electrolyte interphase. *Adv. Energy Mater.* **2021**, *11*, 2100046.
[68] Huang, W.; Wang, H. S.; Boyle, D. T.; Li, Y. Z.; Cui, Y. Resolving nanoscopic and mesoscopic heterogeneity of fluorinated species in battery solid–electrolyte interphases by cryogenic electron microscopy. *ACS Energy Lett.* **2020**, *5*, 1128–1135.
[69] Kim, Y. J.; Kwon, S. H.; Noh, H.; Yuk, S.; Lee, H.; soo Jin, H.; Lee, J.; Zhang, J. G.; Lee, S. G.; Guim, H. et al. Facet selectivity of Cu current collector for Li electrodeposition. *Energy Storage Mater.* **2019**, *19*, 154–162.
[70] Xu, N.; Li, L. L.; He, Y.; Tong, Y.; Lu, Y. Y. Understanding the molecular mechanism of lithium deposition for practical high-energy lithium-metal batteries. *J. Mater. Chem. A* **2020**, *8*, 6229–6237.
[71] Qin, L. G.; Wu, Y. C.; Shen, M. Y.; Song, B. R.; Li, Y. H.; Sun, S. Q.; Zhang, H. Y.; Liu, C. F.; Chen, J. Straining copper foils to regulate the nucleation of lithium for stable lithium metal anode. *Energy Storage Mater.* **2022**, *44*, 278–284.
[72] Gao, X. W.; Zhou, Y. N.; Han, D. Z.; Zhou, J. Q.; Zhou, D. Z.; Tang, W.; Goodenough, J. B. Thermodynamic understanding of Li-dendrite formation. *Joule* **2020**, *4*, 1864–1879.
[73] Shen, C.; Gu, J. L.; Li, N.; Peng, Z. L.; Xie, K. Y. Single crystal Cu (110) inducing lateral growth of electrodeposition Li for dendrite-free Li metal-based batteries. *J. Power Sources* **2021**, *501*, 229969.